Eur. Phys. J. D **6**, 383–396 (1999)

THE EUROPEAN PHYSICAL JOURNAL D

EDP Sciences

Numerical simulations of the nonlinear propagation of femtosecond optical pulses in gases

A. Chiron[1], B. Lamouroux[2], R. Lange[2], J.-F. Ripoche[2], M. Franco[2], B. Prade[2], G. Bonnaud[3], G. Riazuelo[3], and A. Mysyrowicz[2,a]

[1] Dipartimento di Fisica, Università di Pisa, Piazza Torricelli 2, 56100 Pisa, Italy
[2] Laboratoire d'Optique Appliquée, Centre National de la Recherche Scientifique UMR 7639, ENSTA-Ecole Polytechnique 91761 Palaiseau Cedex, France
[3] Commissariat à l'Energie Atomique, DPTA, BP 27, 91680 Bruyères-le-Châtel, France

Received: 19 June 1998 / Received in final form: 14 January 1999

Abstract. A two-dimensional axisymmetric model of the propagation of intense femtosecond laser pulses through dispersion-free transparent media is described. The effects of diffraction, nonlinear Kerr effect (instantaneous and retarded) and multiphoton ionisation are included. Numerical results concerning air and other gases are discussed. In particular, time self-compression of femtosecond pulses is predicted. Stable self-guided pulses are simulated, in agreement with recent experimental observations.

PACS. 42.65.Tg Optical solitons; nonlinear guided waves 42.65.-k Nonlinear optics 52.35.Mw Nonlinear waves and nonlinear wave propagation (including parametric effects, mode coupling, ponderomotive effects, etc.)

1 Introduction

Lasers delivering sub-picosecond pulses with peak powers reaching several terawatts are currently in operation in several laboratories.

In many end-users applications, such as the generation of ultrashort secondary sources [1,2], it is very important to be able to predict how the electromagnetic field of the pulses evolves as it propagates, starting from a location where the field is well determined. This can be computed relatively simply with linear codes as long as the beam propagates in vacuum. However, in many cases, the beam must cross transparent nonlinear media, for instance air or optical windows. This can lead to important changes of the beam characteristics such as pulse shortening, pulse splitting and beam filamentation [3,4]. Within some approximations, analytical solutions can be found [5–7] in a few restricted cases to describe the modification of the pulse; for instance, the "moving focus" model [1,8,9] explains rather well many features also observed with nanosecond pulses. However, in most situations, analytic approximations are useless and one must resort to a more elaborate propagation code.

Several nonlinear propagation codes have been developed so far, generally for plasma studies such as modelling of long-pulses propagation in both inertial confinement fusion and ultra high intensity pulses contexts. In some codes, transverse effects such as diffraction and self-focusing are taken into account within a steady-state approximation [10–12]. In other cases, transverse effects are not included, so that the beam is considered as one-dimensional. Such codes are adequate for the propagation of the beam in optical fibres [13]. Ionisation of the medium at high intensity considerably complicates the problem because it couples space and time. When dealing with ultrashort pulses, the dynamics of the retarded Kerr response brings an additional difficulty. Very recently, several groups have reported results from a genuine 3-D or 2-D axisymmetric code describing the nonlinear propagation of intense femtosecond pulses. Kandidov and Brodeur [14–16] have considered nonlinear propagation with ionisation and instantaneous Kerr effect. Their code is suitable for laser intensities less than $10^{16}\,\mathrm{W/cm^2}$. Mlejnek *et al.* and Ranka *et al.* [17] have reported on a more elaborate form of a similar code, including instantaneous optical Kerr effect, group velocity dispersion, absorption, ionisation and self-steepening. Borisov *et al.* [12] and Mora *et al.* [18–20] have developed codes suitable for the propagation of ultra intense laser pulses (with intensities above $10^{17}\,\mathrm{W/cm^2}$). They adopt a "particles-in-cell" approach to describe the relativistic motion of electrons within a strongly ionised plasma.

In this paper we describe in detail a 2-D axisymmetric propagation code valid in the intermediate intensity range ($I < 10^{15}\,\mathrm{W/cm^2}$). It includes the nonlinear Kerr effect which can be instantaneous and/or retarded [21] as

[a] e-mail: mysy@enstay.ensta.fr

well as the ionisation of the medium through multiphoton absorption or field ionisation. It calculates the spectrum, the time and spatial profiles of the beam at any location. Propagation of pulses can be computed over distances of several of meters within a reasonable time (typically a few hours on a workstation). Group velocity dispersion is not included, so that the code in its present form is applicable only to propagation in gases, for a limited distance. We also neglect losses due to ionisation[1]. We believe that the present code, despite its limitations can be very useful for such problems as the determination of optimal conditions for filamentation and energy coupling to the self-guided pulse.

Section 2 describes the model in detail. Section 3 presents the numerical techniques. Sect 4 shows results of simulations within conditions close to experimental ones.

2 Theoretical model

2.1 Pulse propagation

The propagation of an intense femtosecond laser pulse in a gas involves linear diffraction, linear and nonlinear refraction as well as ionisation of the gas. The refractive index of a neutral gas varies as a function of the local laser intensity $I(z,r,t)$, where z denotes the propagation axis, r the transverse axis and t the time. The electric field $\mathcal{E}$ is expressed as a quasi-plane wave propagating towards increasing z:

$$\vec{\mathcal{E}}(z,\vec{r},t) = \vec{E}(z,\vec{r},t)e^{-i\omega_0 t+ik_0 z} + \text{c.c}\,, \qquad (1)$$

where $\vec{E}$ denotes the slowly varying envelope as complex quantity, ω_0 and k_0 are the radial frequency and the wave vector of the incident carrier wave in the medium, respectively.

If the pulse polarisation is unmodified, we are left with a scalar paraxial equation:

$$2i\left(\frac{1}{\omega_0}\frac{\partial E}{\partial t} + \frac{k_0 c^2}{\omega_0^2}\frac{\partial E}{\partial z}\right) + \Delta\varepsilon E + \frac{c^2}{\omega_0^2}\nabla_\perp^2 E = 0\,. \qquad (2)$$

Here $\Delta\varepsilon = 2N_0\Delta N$ represents the modification of the dielectric permitivity, where N_0 is the linear index of the medium and ΔN, the nonlinear index, is assumed to be much smaller than N_0. $\perp$ denotes the transverse coordinate. By using the normalized quantities $\eta = z/(c/\omega_0)$, $\tau = \omega_0 t - \eta\omega_0/k_0 c$ and $\tilde{\perp} = \tilde{r} = r/(c/\omega_0)$, the equation of the electric field $E(\eta,\tau)$ becomes:

$$2i\frac{k_0 c}{\omega_0}\frac{\partial E}{\partial \eta} + \nabla_{\tilde{r}}^2 E + \Delta\varepsilon E = 0\,. \qquad (3)$$

In this equation,

- the term $\partial E/\partial\eta$ represents the electric field evolution along the propagation axis,
- the term $\nabla_{\tilde{r}}^2 E$ represents the linear diffraction,
- the third term of equation (2) denotes the nonlinear variation of the index of the medium, or equivalently the coupling between the medium and the pulse.

This equation is based on the following approximations:

a) The slowly varying envelope approximation by neglecting the second derivative $\partial^2 E/\partial t^2$ compared to $\omega_0\partial E/\partial t$. This restricts the validity of the code to pulse durations of the order of, or larger than, 10 fs in the visible range.

b) The group velocity dispersion is neglected. Group velocity is proportional to $\partial^2 E/\partial t^2$ and becomes important even in gaseous media away from a resonance, when ultrashort pulses are used. For example, a 10 fs pulse at 800 nm experiences a broadening due to group velocity dispersion of $\sqrt{2}$ over a distance of 10 meters in argon.

c) The paraxial approximation: this restricts the validity of the code to small divergences of the beam ($k_\parallel < k_\perp$) and slow axial variations over the wavelength scale λ_0. Consequently, no reflection is considered.

d) The electric field is always pure transverse ($\vec{\nabla}\times\vec{\mathcal{E}} = 0$).

e) For the Kerr nonlinearity, we assume that a perturbation expansion in successive orders of the electric field is valid.

f) We consider only underdense plasmas. The free electron density is assumed to be small compared to both the atomic density $\mathcal{N}_{00}$ and the critical density n_c that makes the plasma opaque. The critical density is given by the expression $n_c = 10^{12}/\lambda_0^2$ with the density in units of cm^{-3} and λ_0 in m.

The nonlinear index ΔN is expressed as a superposition of free electron contribution (corresponding to the plasma effects) and bound electron contribution (representing the nonlinear Kerr effect):

$$\Delta N = \Delta N_{\text{Kerr}} - \frac{\omega_p^2}{2\omega_0^2}\,, \qquad (4)$$

where $\omega_p^2(t) = n_f(t)e^2/m_e\varepsilon_0$ denotes the radial electron plasma frequency, with $n_f(t)$ the time varying free electron density, $-e$ the electron charge, m_e the electron mass and ε_0 the dielectric permitivity of vacuum.

g) Losses due to multiphoton ionisation have been neglected. Over a propagation distance of a few meters after the start of filamentation such losses are relatively small and hence will not affect significantly the numerical results.

2.2 Plasma contribution

The plasma contribution to the non-linearity is first examined. One must calculate $n_f(t)$ in order to have the second term on the right hand side of equation. (4). $n_f(t)$

[1] In a more complete model, that we have developed recently, losses have been incorporated together with group velocity dispersion. This new version of our code requires a tenfold increase of the computing time. We find little differences between both versions of the code as long as the propagation distance after the onset of ionisation is kept small (less than a few meters).

is given by

$$n_{\mathrm{f}}(t) = \sum_k k\mathcal{N}_k \,, \tag{5}$$

$\mathcal{N}_k$ is the density of atoms with charge $-ke$.

Before the interaction with the pulse, the gas is assumed to be electrically neutral with atom density $\mathcal{N}_{00}$. During the pulse, ions are created. The charge density of atoms changes according to

$$\frac{\mathrm{d}\mathcal{N}_k}{\mathrm{d}t} = w_{k-1}\mathcal{N}_{k-1} - w_k\mathcal{N}_k \,, \tag{6}$$

where k is the degree of ionisation of the atom, w_k represent the ionisation rate of the atom with charge $-ke$. The ionisation rate w_k is a function of the laser intensity. Here we neglect collisional ionisation which is negligible in the intensity and gas density regime that we consider ($I \leq 10^{15}\,\mathrm{W/cm^2}$).

Depending on the laser intensity the creation of free electrons is described by one of the following models: the multiphoton ionisation model or the tunnel ionisation model.

The separation between these regimes is given by the Keldysh constant Γ defined by [22]:

$$\Gamma_k = \left[\frac{U_k}{2\mathcal{V}}\right]^{1/2} , \tag{7}$$

where U_k is the ionisation potential of one atom and $\mathcal{V}$ the quiver energy of a free electron in the laser field; $\mathcal{V} = eE^2/4m_{\mathrm{e}}\omega_0^2$. For $\Gamma < 1$ the tunnel regime is dominant whereas for $\Gamma > 1$ the multiphoton regime is the strongest effect. In the multiphoton regime which applies to intensities below $10^{14}\,\mathrm{W/cm^2}$, the ionisation rate is given by

$$w_k = \sigma_{pk} I^p \,, \tag{8}$$

where p is the number of photons required to reach the ionisation of a given level k with potential U_k given in eV as

$$p = eU_k/h\nu \,. \tag{9}$$

In the tunnel regime, above $10^{14}\,\mathrm{W/cm^2}$ we adopt the A.D.K. model valid for a linearly polarised incident field [22–26]:

$$w_k = \left[\frac{3}{\pi}\left(\frac{U_k}{U_{\mathrm{H}}}\right)^{3/2}\frac{E}{E_{\mathrm{at}}}\right]^{1/2} w_{i,k}(E) \,, \tag{10}$$

with

$$w_{i,k} = \frac{\omega_{\mathrm{at}}}{2} C_{n^*}^2 \frac{U_k}{U_{\mathrm{H}}}\left[2\left(\frac{U_k}{U_{\mathrm{H}}}\right)^{3/2}\frac{E_{\mathrm{at}}}{E}\right]^{2n^*-1} \times \exp\left[-\frac{2}{3}\left(\frac{U_k}{U_{\mathrm{H}}}\right)^{3/2}\frac{E_{\mathrm{at}}}{E}\right] ,$$

$$n^* = Z\sqrt{\frac{U_{\mathrm{H}}}{U_k}}, \text{ and } C_{n^*} = \left(\frac{2\exp(1)}{n^*}\right)^{n^*}\frac{1}{\sqrt{2\pi n^*}} \,.$$

Z is the charge number of the ion, $E_{\mathrm{at}} = 5.142{\cdot}10^{11}\,\mathrm{V/m}$ is the characteristic electric field strength on the first Bohr orbit of the hydrogen atom, $\omega_{\mathrm{at}} = 4.16 \cdot 10^{16}\,\mathrm{s^{-1}}$ is the gyration radial frequency of that first Bohr orbit, $U_{\mathrm{H}} = 13.6$ eV is the ionisation potential of hydrogen.

2.3 Kerr nonlinearity

The nonlinear refractive-index coefficient of the medium is expressed as

$$n_{\mathrm{I}} = \sum_k \mathcal{N}_k n_{2,k} \,, \tag{11}$$

where $n_{2,k}$ is the nonlinear coefficient of one atom ($k = 0$) or one ion with charge $-ke$ ($k > 0$). Compared to the instantaneous response of a neutral atom, the instantaneous Kerr response of an ion represents a few percents and will be neglected. The nonlinear refractive-index coefficient can be then reduced to

$$n_I(t) = \mathcal{N}_0(t) n_{2,0} \,. \tag{12}$$

In order to describe the presence of retarded response, the nonlinear index can be written as

$$\Delta N_{\mathrm{Kerr}} = n_{\mathrm{I}} I(t) + n_{\mathrm{R}} \int_{-\infty}^{t} R(t-t')I(t')\mathrm{d}t' \,, \tag{13}$$

where R denotes the time-retarded response of the medium, and n_{I}, n_{R} the respective strengths of the instantaneous and the delayed Kerr effects. The instantaneous Kerr effect corresponds to the nonlinear distortion of the electron cloud and takes place over time scale $\tau \approx 10^{-15}\,\mathrm{s}$ in all materials. The retarded Kerr effect is associated with a nuclear motion. It has been shown in references [27] and [28] that the retarded response in the air corresponds to the dephasing of an initial coherent superposition of a limited set of rotational states of molecules. Its kinetics can be quite complex [27,28]. Here it will be simply modelled by the following expression [7,9,29]:

$$n_{\mathrm{R}} \int_{-\infty}^{t} R(t-t')I(t')\mathrm{d}t' = \frac{n_{\mathrm{R}}}{\tau_{\mathrm{K}}} \int_{-\infty}^{t} e^{-(t-t')/\tau_{\mathrm{K}}} I(t')\mathrm{d}t' , \tag{14}$$

with a simple exponential relaxation time τ_K of 70 fs, approximating closely the measured response.

3 Numerical method

We use the code PARAX [10] redefined with a Crank-Nicholson scheme which is an implicit finite-difference method recognised as conditionless stable. The continuous field $E(z,r)$ is represented on a regular grid with mesh size Δz and Δr along axial and transverse directions, respectively.

Henceforward, axisymmetry around the propagation axis z is assumed. We have: $\Delta\xi = \Delta\eta\omega_0/k_0 c$, $\tilde{r} = (m-1)\Delta\tilde{r}$.

Let us now examine the different terms in equation (3):

– the first term is approximated by:

$$\frac{\partial E}{\partial \xi} = \frac{E_{n,m} - E_{n-1,m}}{\Delta\xi}, \qquad \forall\, n \in [1, N_z]\,, \tag{15}$$

– the diffraction term in cylindrical geometry has to be carefully discretised since quantity $(1/r)\partial/\partial r(r\partial E/\partial r)$ diverges for small r. For the central value of E ($r = 0$), we replace $\nabla^2_{\tilde{r}} E$ by

$$\frac{4}{\Delta\tilde{r}^2}(E(\Delta\tilde{r}) - E(0)) = \frac{4}{\Delta\tilde{r}^2}[E_{n,2} - E_{n,1}]\,. \tag{16}$$

For $r > 0$, the first derivative term is approximated by: $\frac{1}{r}\frac{\mathrm{d}E}{\mathrm{d}r} \approx \frac{E_{n,m+1} - E_{n,m-1}}{2r_m \Delta r}$, so that the full transverse diffractive term $\nabla^2_\perp = \frac{1}{r}\frac{\partial}{\partial r}(r\frac{\partial E}{\partial r})$ is then given by

$$\frac{1}{\Delta\tilde{r}^2}\left[\left(1 + \frac{1}{2(m-1)}\right) E_{n,m+1} + \left(1 - \frac{1}{2(m-1)}\right) E_{n,m-1} - 2E_{n,m}\right]. \tag{17}$$

According to the Crank-Nicholson scheme, the field E is given by $E = [E(\eta + \Delta\eta) + E(\eta)]/2$.

– Assuming that the variations of ΔN are always small compared to N_0 during each propagation step $\Delta\eta$, the induced change of index is then approximated as

$$\Delta N\left(\frac{E(\eta + \Delta\eta) + E(\eta)}{2}\right) \cong \Delta N(E(\eta))\,.$$

By introducing the change of notations: $\eta_1 = \frac{i\Delta\xi}{2\Delta\tilde{r}^2}$, $p_\pm = 1 \pm 2\eta_1$, $u_m = 1/(2(m-1))$, equation (3) becomes

$$\begin{aligned} &E_{n,m}\left[p_+ - \frac{i\Delta\xi}{2}\Delta\varepsilon\right] - \eta_1[(1+u_m)E_{n,m+1} \\ &\quad +(1-u_m)E_{n,m-1}] = \\ &E_{n-1,m}\left[p_- + \frac{i\Delta\xi}{2}\Delta\varepsilon\right] + \eta_1[(1+u_m)E_{n-1,m+1} \\ &\quad +(1-u_m)E_{n-1,m-1}]\,. \end{aligned} \tag{18}$$

We now address the time variation. For each value of η, the time evolution t is discretised into k elements t_k. The Crank-Nicholson scheme is applied to each time element. The Kerr effect and the ionisation effect can be written as integral responses, so that their time contribution can be reduced to a simple product at each time t_k.

To stay whithin a reasonable computing time, the full size of the time axis is taken as typically 10 times the pulse duration and the length of the radial axis is 5 times the beam waist; pulse duration and waist refer to $1/e^2$ of the intensity peak. To avoid artifacts due to reflections at the box boundaries, we impose absorption conditions for outgoing fields.

The input beam can be introduced in two ways: in an analytic form or as a data table. The pulse is defined by the product of two functions: $E(r,t) = f(r) \times g(t)$, where $f(r)$ represents the input spatial profile and $g(t)$ the input temporal part. The spatial part is usually assumed to be Gaussian but can also reproduce an experimental profile measured with a beam profile analyser. The time part is assumed to have a sech^2 shape or a Gaussian shape or can be deduced from the experimental measurements of light spectra, assuming a given spectral phase profile.

As diagnostics, the code provides the beam intensity at each point (z,r), as well as the associated frequency spectrum. In addition, the local free electron density and the effective refractive index are given. Finally at each axial location z, the beam size is defined as the Full Width at Half Maximum (FWHM) of the fluence $F(z, r=0) = \int_{-\infty}^{\infty} I(z, r=0, t)\mathrm{d}t$, which is the time-integrated energy over the whole pulse, a quantity experimentally accessible[2].

4 Numerical results

In order to identify the influence of the different physical processes coming into play, they are introduced successively, keeping the same input conditions. A standard input beam typical of Ti:Sapphire laser emitting at $\lambda_0 = 800$ nm is adopted for the different situations:

$$I(r,t) = I_0 \exp(-2r^2/w_0^2)\mathrm{sech}^2(at/\tau)\,, \tag{19}$$

where $a = \ln(1+\sqrt{2})$. We have chosen $\tau = 120$ fs as the input duration of the pulse, $w_0 = 2$ mm as the beam waist and $I_0 = 2 \cdot 10^{11}\,\mathrm{W/cm^2}$ as the peak irradiance. These parameters lead to a total pulse energy of 2 mJ for an incident power peak $P_0 = I_0 \int_0^\infty \exp(-2r^2/w_0^2) 2\pi r\,\mathrm{d}r$ close to $1.3 \cdot 10^{10}\,\mathrm{W}$. In most cases, the initial temporal phase $\Psi(t)$ and spatial phase $\Phi(r)$ are assumed to be constant. However, we will consider explicitly a case with an initial quadratic spatial phase. The propagation of a collimated beam (a parallel beam) through a dispersionless medium with instantaneous Kerr response, then through a Kerr medium with instantaneous and retarded nonlinear response and finally the same cases in the presence of ionisation are considered. For the sake of clarity, a full display of the pictures ($-r_{\max} \le r \le r_{\max}$) instead of a symmetric display ($0 \le r \le r_{\max}$) is used.

To complete a run with physical interest, 15 hours of a Hewlett-Packard C160 workstation are necessary, with typically 128 points to describe the time profile, 2000 points to define the radial extension and at least 1000 points along the propagation axis.

4.1 Instantaneous Kerr effect alone

The instantaneous nonlinear Kerr effect alone is first considered, with $n_\mathrm{I} = 3.2\ 10^{-23}\,\mathrm{m^2/W}$, typical of xenon at

[2] We introduce this unusual definition of the beam diameter in order to accommodate for pulse splitting. The usual definition in terms of intensities becomes meaningless for structured time-profiles. However, it is always possible to define the beam diameter in terms of fluence.

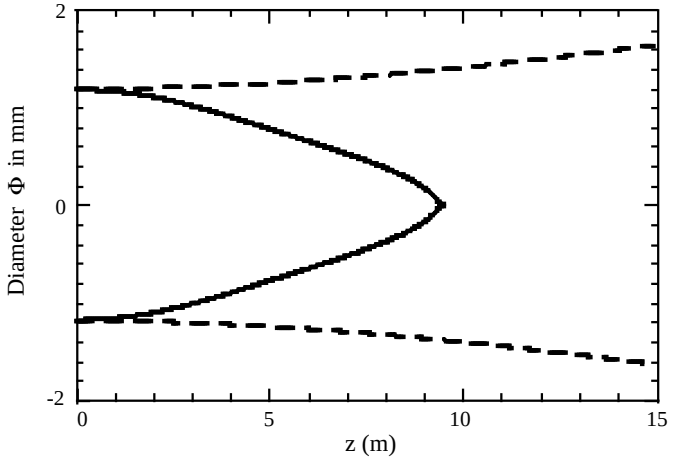

Fig. 1. Beam diameter as a function of the propagation distance z in the case of pure instantaneous Kerr effect (continuous lines), and in the case of pure diffraction only (dashed lines).

atmospheric pressure. Figure 1 shows the well-known self-focusing effect of the beam. After a finite propagation distance from departure, the laser pulse collapses to a zero diameter: beyond this point, no physical representation is then possible. The solid lines represent the size (FWHM) of the beam as described at the end of Section 3. Also shown is the pulse propagation in vacuum (dashed lines) over a distance close to the Rayleigh length given by $z_{\mathrm{R}} = \pi w_0^2/\lambda_0 = 15.7$ m with the initial parameters. In Figure 2(a) the incident power P_0 exceeds the critical power for instantaneous Kerr self-focusing effect $P_{\mathrm{c}} = 1.5{\cdot}10^{-10}\lambda_0^2/n_{\mathrm{I}} = 3$ GW, with λ_0 and n_{I} in M.K.S.A. units. We have deliberately chosen a ratio $P_0/P_{\mathrm{c}} = 4.3$ as a representative case where the condition for self-focusing is well satisfied. Figure 2(b) shows the distance of the critical focus as a function of time during the pulse duration: because of the temporal variation of the intensity during the ascending and descending part of the pulse, the focal distance varies with time. The result of our numerical simulation (continuous line) is compared to the semi-analytical expression obtained in the frame of the moving focus model [1–9] (dashed line):

$$z_{\mathrm{f}} = \frac{0.367 k_0 w_0^2}{\left[\sqrt{\dfrac{P_0}{P_{\mathrm{c}}}} - 0.852\right]^2 - 0.0219}\,. \qquad (20)$$

The deviation between the present numerical calculations (full line) and the analytical solution given by equation (20) (dashed line) shows that the semi-analytical solution is a good approximation only for values of P_0 greater than $3P_{\mathrm{c}}$. However, significant deviation amounting to more than 50% are visible on the rising and falling edges of the pulse.

Figure 3 shows the spectrum associated with the propagating pulse at various distances. As the beam propagates through the medium, the phase of the pulse is modified by the Kerr nonlinearity. The question sometimes

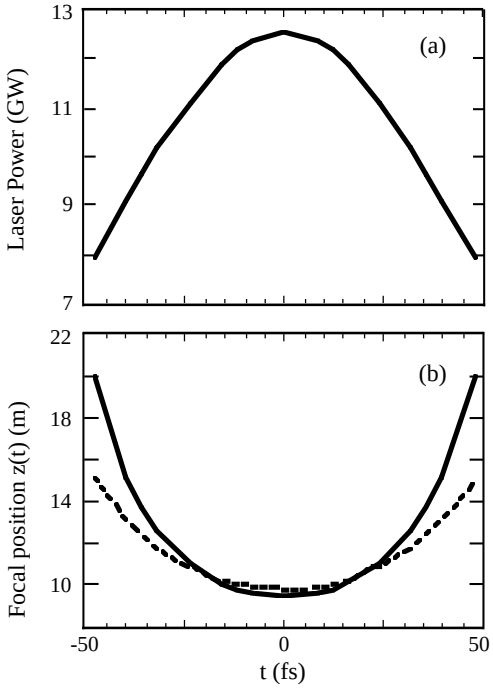

Fig. 2. (a) Initial power at $z = 0$ m as a function of time. (b) Location of the focal point of each time slice of the pulse (continous line) for a pure instantaneous Kerr effect. The theorical curve [9] is the dashed one.

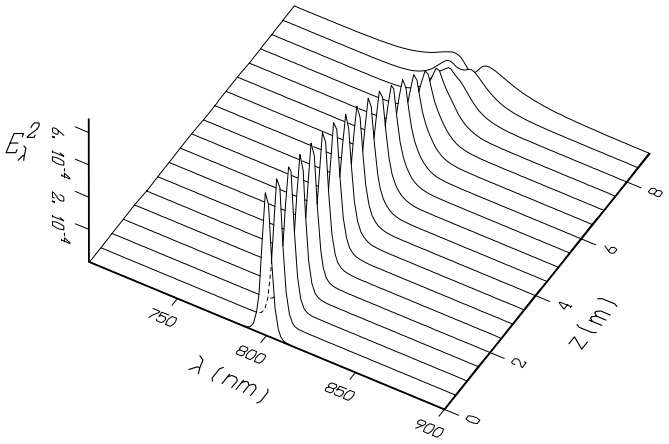

Fig. 3. Spectral shape evolution of the pulse *versus* the propagation distance z for a pure instantaneous Kerr effet. The field is radially integrated over a 160 μm diameter.

arises about the respective importance of the spectral and spatial changes to this total phase variation. In fact, it depends on the initial beam conditions. To illustrate this assertion Figure 4(a) compares the beam size evolution for two pulses with same peak intensities but with different waists. The distance corresponding to the same spectral amplitude modifications, as shown in Figure 4(b), is shown by the two arrows. As can be seen, in one case the beam diameter has shrinked to nearly half its initial size whereas in the second case the beam is reduced by less than 10%. This point is important since it allows

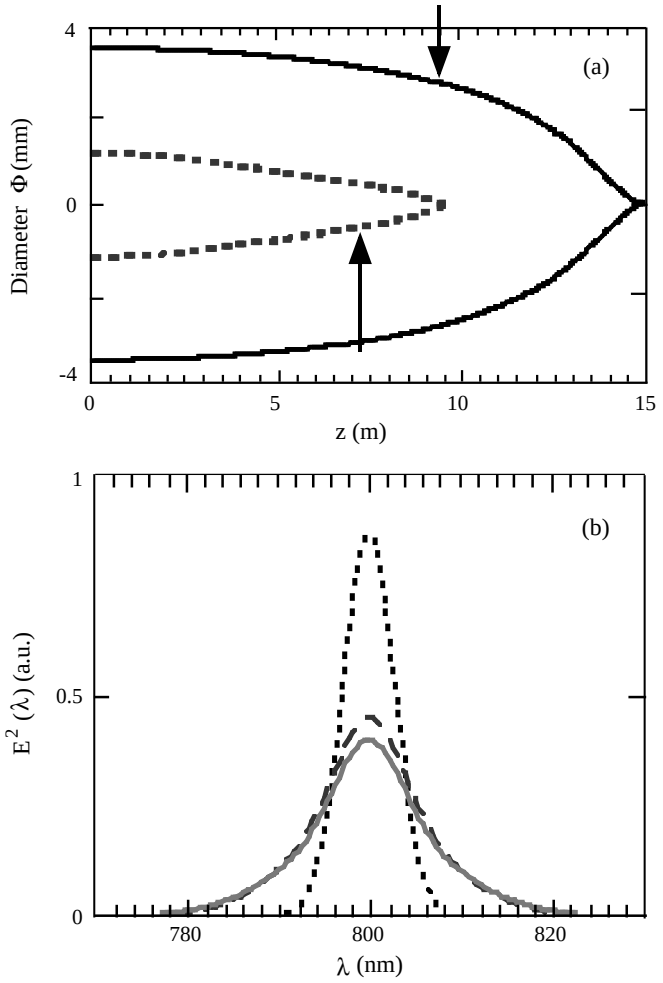

Fig. 4. (a) Full width at half maximum energy in pure instantaneous Kerr effect, for a 6 mm waist (continous lines) and a 2 mm waist (dotted lines). The arrows are representing the positions where the (b) spectra have been recorded. (b) Comparisons between the spectra recorded at $r = 0$ for $z = 0$ (dotted line), for $z = 7$ m (dashed line) with a 2 mm waist, and for $z = 8$ m (continuous line) for a 6 mm waist.

to validate an assumption made in some phase retrieval methods [30–33] *i.e.* that spatial changes are negligible for power ratio $P_0/P_c \leq 3$.

The pulse time shape is now examined as a function of distance. A shorter pulse is obtained close to (and in the vicinity of) the axis since an intensity-dependent transfer of energy occurs from the outer parts of the beam to the centre keeping the initial time-symmetry of the pulse. This effect is illustrated in Figure 5 where the on-axis intensity is plotted as a function of distance. By putting a diaphragm along the path of the beam in the vicinity of z_f, self-focusing could perhaps be exploited to reduce the initial pulse duration[3].

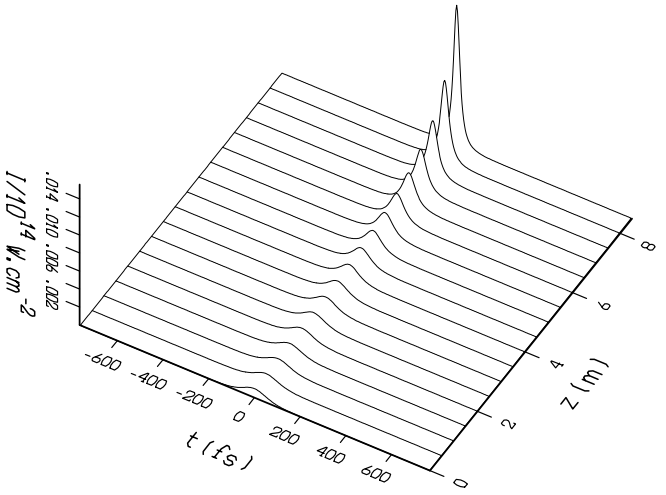

Fig. 5. Time profile of the pulse as a function of the propagation distance z for a pure instantaneous effet Kerr. The field is radially integrated over a 160 μm diameter.

To stress this point, the expected pulse reduction is shown in Figure 6(a) as a function of diaphragm position for a diaphragm of 8 μm (dotted line) and 16 μm diameter (continuous line), for the same condition as in Figure 1. In Figure 6(b), the fraction of transmitted energy is plotted as a function of distance for the same diaphragm sizes. In the case of the 160 μm diameter diaphragm (full line), the transmitted energy is significant showing that this effect can lead to a practical scheme for the reduction of femtosecond pulses.

4.2 Retarded Kerr response

In many cases, the nonlinear Kerr effect originates from both electrons and nuclear motion. Well-known examples are found in the literature for polar liquids such as CS_2 [34], molecular gases [35], and air more specifically [36–38]. This type of Kerr effect is characterised by a response time which can exceed several tens of femtoseconds. Here we will assume that it can be cast in the form described by equation (13).

To enlighten the effect of a retarded response, we have simulated the time, space and spectrum evolutions of a pulse with the value of $n_I + n_R = 3.2 \cdot 10^{-23}\,m^2/W$ for three values of the ratio $r_K = n_R/n_I$, keeping $n_I + n_R$ constant. The third case approximates the air at half the standard pressure. The decay constant τ_K is taken as 70 fs.

Figure 7(a) shows how the beam diameter evolves as a function of the ratio r_K due to self-focusing. The instantaneous Kerr effect ($r_K = 0$) is represented by the dotted curve. The added retarded Kerr effect is plotted by a dashed curve ($r_K = 0.2$) or a continuous line ($r_K = 1$). In practice the ratio of n_R/n_I can be changed by mixing

[3] Evidence for pulse shortening in the pure Kerr region has been observed recently in our group (R. Lange, Thesis, Ecole Polytechnique, 1998). According to the numerical results, the pulse duration diminishes if one reduces the aperture down to the filament size. Below this diameter, the pulse duration stays constant. We could demonstrate experimentally that the pulse duration is shorter in the filament, but could not resolve time profiles within the filament (Lange *et al.*, to be published).

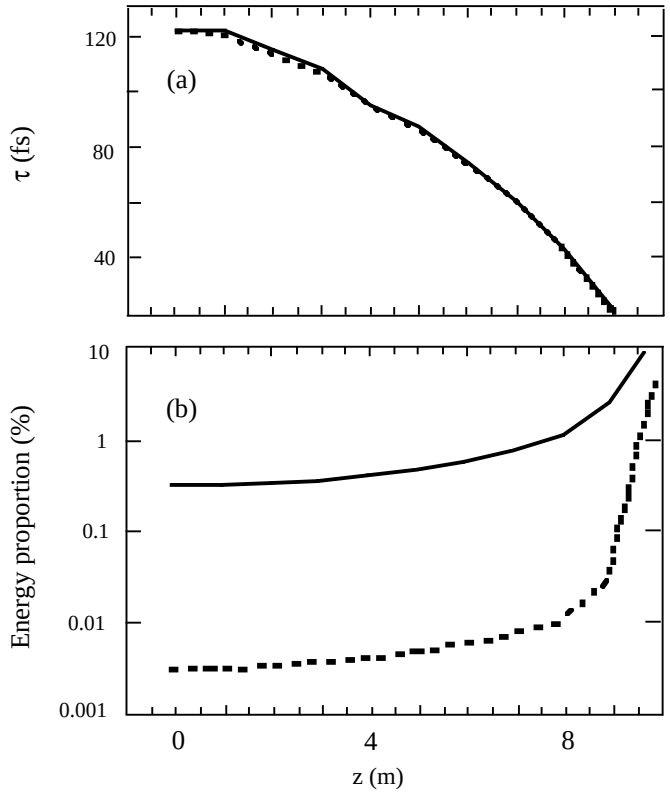

Fig. 6. (a) Pulse duration *versus* the propagation distance. For a pure instantaneous Kerr effect, we have two radial integration over a 8 μm diameter (dotted line) and a 160 μm diameter (continuous line). (b) Energy density transmission in the center of the filament with a radial integration over 8 μm diameter (dotted line) and 160 μm diameter (continuous line).

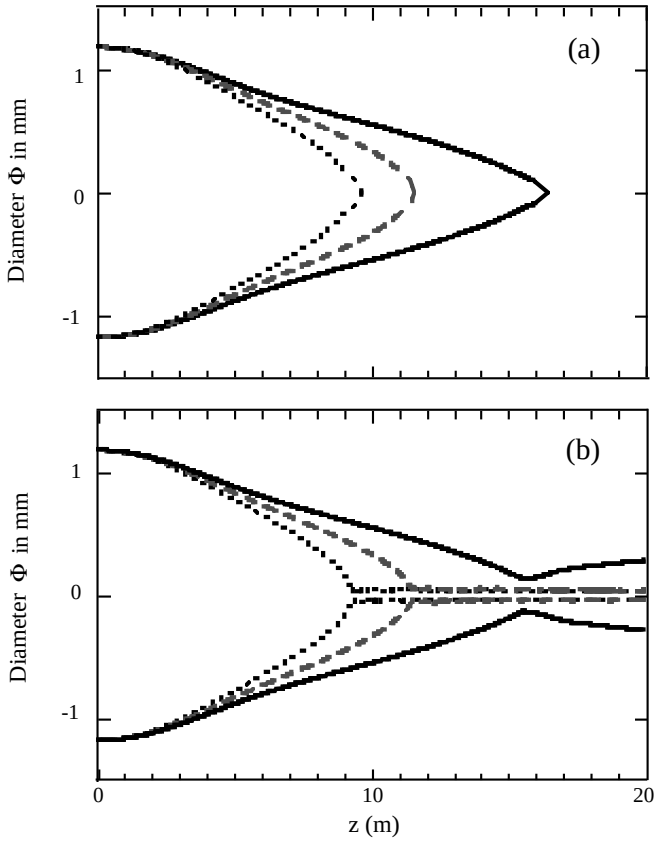

Fig. 7. (a) Evolution of the beam diameter with the propagation distance for $r_{\mathrm{K}} = 0$ (dotted lines), $r_{\mathrm{K}} = 0.2$ (dashed lines) and $r_{\mathrm{K}} = 1$ (continuous lines). The nonlinear index includes instantaneous and retarded Kerr effect. (b) Evolution of the beam diameter with the propagation distance for $r_{\mathrm{K}} = 0$ (dotted lines), $r_{\mathrm{K}} = 0.2$ (dashed lines) and $r_{\mathrm{K}} = 1$ (continuous lines). The nonlinear index includes instantaneous and retarded Kerr effect, and ionisation.

molecular gases (N_2, O_2, CO_2) with noble gases which have an instantaneous response only. The main consequence of the retarded effect is that the critical distance for beam collapse appears to be increased when compared to the case of instantaneous response only. The physical reason for this behavior is the following. Since $n_{\mathrm{I}} + n_{\mathrm{R}}$ is kept constant, the effective nonlinear index in the presence of a retarded response is decreased at early times. As a consequence, the peak effective nonlinear index is decreased, compared to the pure instantaneous case and the focal length increased according the rough rule $z_{\mathrm{f}} \propto n_{\mathrm{I}}^{-1/2}$.

4.3 Ionisation

As we have seen in Section 2.2 once the laser intensity is in excess of $10^{13}\,\mathrm{W/cm^2}$ there is an important probability that the gas becomes ionised. This ionisation leads to a reduction of the refractive index (see Eq. (4)) and consequently the propagation is deeply modified.

In the intensity range prevailing here, the plasma consists of singly ionised atoms only. The system of equations (5) is then reduced to

$$\frac{\mathrm{d}\mathcal{N}_0}{\mathrm{d}t} = -w_0(t)\mathcal{N}_0 \tag{22a}$$

for nonionised gas and

$$\frac{\mathrm{d}\mathcal{N}_1}{\mathrm{d}t} = w_0(t)\mathcal{N}_0 \tag{22b}$$

for singly ionised atoms. So, we have

$$\mathcal{N}_0(t) + \mathcal{N}_1(t) = \mathcal{N}_0(t=0) = \mathcal{N}_{00}\,, \tag{23}$$

which expresses the conservation of the number of electrons in the medium. $\mathcal{N}_{00}$ is the maximum electron density which can be ionised. $w_0(t)$ represents the ionisation probability which depends on the laser intensity I and $\mathcal{N}_0(t=0)$ the initial density of neutral atoms.

In order to quantify the ionisation effect, a "hybrid" model is used which combines the multiphoton and the tunnelling model. To fix the value σ_{pk} in equation (8) the ionisation rate is assumed to be fixed by equating the multiphoton rate to the tunnel rate when $\Gamma = 1$. Furthermore, the value $p = 9$ is chosen in equation (9). It corresponds to the number of photons at $\lambda_0 = 800$ nm necessary to make a multiphoton transition in the presence of a ionisa-

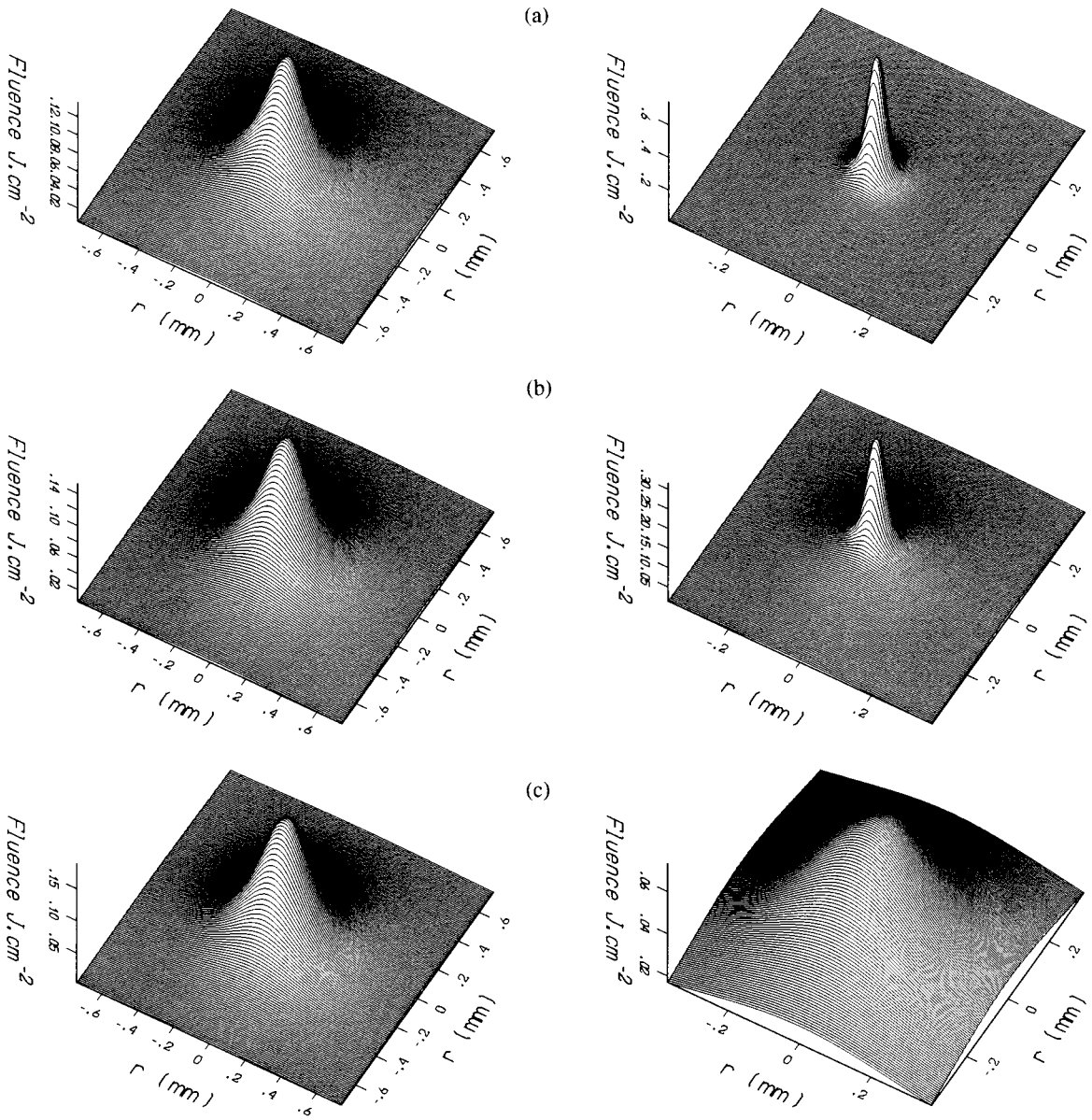

Fig. 8. 3D representation of the fluence of the beam at different distances for three cases corresponding to (a) $r_{\rm K} = 0$, (b) $r_{\rm K} = 0.2$ and (c) $r_{\rm K} = 1$. For each case we have (left) $z = 0.95 z_{\rm f}$ and (right) $z = 1.5 z_{\rm f}$. Note the scale difference between the left and right pictures.

tion potential of 14.6 eV. This value is close to the average ionisation potential of N_2 (15.6 eV) and O_2 (12.1 eV)[4].

Figure 7(b) shows the diameter of the laser beam as a function of distance in the presence of Kerr effect and ionisation as described by equation (4). The dotted line corresponds to a simulation with a pure instantaneous Kerr effect with a value for the Kerr coefficient $n_{\rm I} = 3.2\ 10^{-23}\,{\rm m}^2/{\rm W}$ ($n_{\rm R} = 0$). The dashed curve is obtained in the presence of retarded Kerr effect with the Kerr coefficients $n_{\rm I} = 2.4 \cdot 10^{-23}$ and $n_{\rm R} = 0.8 \cdot 10^{-23}\,{\rm m}^2/{\rm W}$ and a time response of 70 fs for the retarded response (Eq. (14)). The continuous line gives the beam diameter when the instantaneous and retarded Kerr effect have same magnitude $n_{\rm I} = n_{\rm R} = 1.6 \cdot 10^{-23}\,{\rm m}^2/{\rm W}$. The beam is guided in the first two cases with the same filament diameter. However in the third case, the beam is not self-guided due to the decrease of the effective nonlinear index. Figure 8 shows the spatial representations of the energy profile at different distances for the conditions of Figure 7(b). In Figure 8(a,b) the beam is trapped in a self-guiding mode with 100 μm diameter over distances exceeding many Rayleigh lengths. 5 to 10% of the initial energy is trapped in the filament. Inside this filament,

[4] We have run our code with the value 12.1 eV corresponding to the ionisation potential of oxygen and 14.6 eV. Although differences are noticeable on a microscopic scale, the macroscopic features are essentially the same.

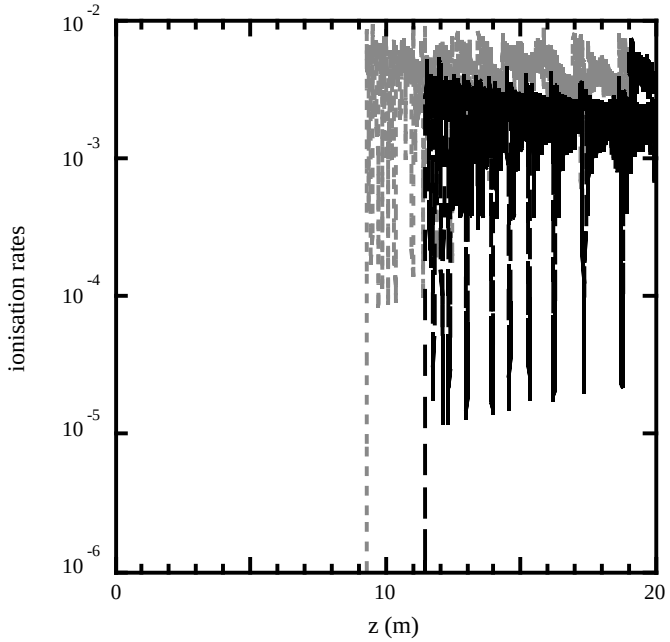

Fig. 9. Evolution of the ionisation rate with the propagation distance z for $r_{\rm K} = 0$ (dotted line), $r_{\rm K} = 0.2$ (dashed line). The case $r_{\rm K} = 1$ does not appear because its maximum amplitude is less than 10^{-11}.

the intensity is limited to a value of a few $10^{13}\,{\rm W/cm^2}$. By contrast, in Figure 8(c), the beam intensity profile increases with distance, since no filamentation occurs.

The crucial role of ionisation for the beam-guiding process is shown in Figure 9. The ionisation rate increases abruptly at the onset of the filament and fluctuates considerably with distance, but it never exceeds a few percent, justifying *a posteriori* the assumption of single stage ionisation. It should be noted that for the same amount of instantaneous and retarded Kerr effects, ionisation although very small ($\approx 10^{-6}$) can still prevent beam collapse, as seen in Figure 7 (cases (a) and (b)).

Figure 10 shows the time profiles as a function of distance in the filamentation regime starting before the focal point, for the three ratios described above. These shapes are integrated over a 160 μm diameter section in order to simulate experimentally accessible quantities. Before the focal point, the pulse durations have been reduced from 120 fs to about 20 to 30 fs. In the presence of instantaneous Kerr effect and ionisation (Fig. 10(a)) the pulse breaks into two shorter pulses with a duration of about 20 fs and a separation increasing with distance. By adding 20% of retarded Kerr effect (Fig. 10(b)) and keeping $n_{\rm I} + n_{\rm R}$ constant, pulse breaking is also observed but the second pulse is less important. With 50% of retarded Kerr effect (Fig. 10(c)) there is no clear appearance of a second pulse; it is replaced by a pedestal on the back part of the pulse. This effect can be seen in Figure 10(e) where the time-intensity profile of the pulse is recorded in the light filament, at $z = 1.05 z_{\rm f}$, where $z_{\rm f}$ is the self-focussing distance defined by equation (20). For comparison, we have plotted in Figure 10(d) the pulse time-shape recorded at $z = 0.95 z_{\rm f}$. The initial time-symmetry of the pulse is suppressed. The peak of the central part of the beam is delayed. The retarded Kerr effect inhibits the pulse shortening discussed in Section 4.1, but leads also to a distortion of the pulse shape, with a steeper leading edge and a smoother trailing edge. The observed pulse splitting is due to ionisation, as confirmed by numerical simulation that we made using a converging beam geometry where the Kerr nonlinear response is switched off. A simple intuitive explanation of how ionisation leads to pulse splitting is not obvious to us.

The corresponding spectra, integrated spatially over a radial diameter of 160 μm, are presented in Figure 11 with the same conditions as in Figure 10. One can observe that self-guiding without retarded Kerr effect (Fig. 11(a)) or with 20% of retarded Kerr effect (Fig. 11(b)) is characterized by strong modulations of the spectra which is evidence for a dramatic distortion of the pulse time profile. The spectral width can extend over a 200 nm range. By equalling instantaneous and retarded Kerr effect (Fig. 11(c)), these strong spectral distortions are replaced by smoother self-phase modulations as shown for $z = 0.95 z_{\rm f}$ in Figure 11(d) and for $z = 1.05 z_{\rm f}$ in Figure 11(e).

4.4 Filament in air

As an application, we now consider the expected behavior of a pulse propagating in air at atmospheric pressure. The propagation of both a collimated beam and a converging beam will be studied. The use of converging beams makes the direct comparison with experiments easier: self-guiding effects can occur within a reasonable distance of a few meters. The initial conditions for the simulation are as follows: the time duration of the pulse is $\tau = 120$ fs, the beam waist is about 2 mm and the peak intensity is $I_0 = 10^{11}\,{\rm W/cm^2}$. These parameters lead to an energy close to 2 mJ. The gas is at atmospheric pressure with Kerr parameters taken as $n_{\rm I} = n_{\rm R} = 3.2 \cdot 10^{-23}\,{\rm m^2/W}$ [28] and $\tau_{\rm K} = 70$ fs [39] for the decay time associated to a single-sided exponential retarded response.

Figure 12 shows the beam profile of an initially collimated beam. The filament appears at the distance 6.40 m, close to the experimental observation [38,40]. The calculated filament diameter $\Phi = 100$ μm is also in agreement with experiments [39]. A ring pattern can be seen (Fig. 12(c)-(f)) after the onset of the filament. As already stressed by Kosareva *et al.*, these rings are connected with surges of ionization and are most probably at the origin of the observed conical emission reported in reference [38]. Figure 13 shows the time/space profile of the beam intensity at different distances before the onset of the filament (panel (a), $z = 6$ m) and behind (panel (b), $z = 6.5$ m) the guiding onset distance. In contrast to the case of Figure 10(c), more than one pulse survives. Note that the pressure is twice the pressure of the corresponding case in Figure 10(c), hence the difference in the pulse profile.

With a focal length $f = 2$ m, a converging beam behaves similarly in terms of filament size, intensity and pulse squeezing (Fig. 14) as a freely propagating beam.

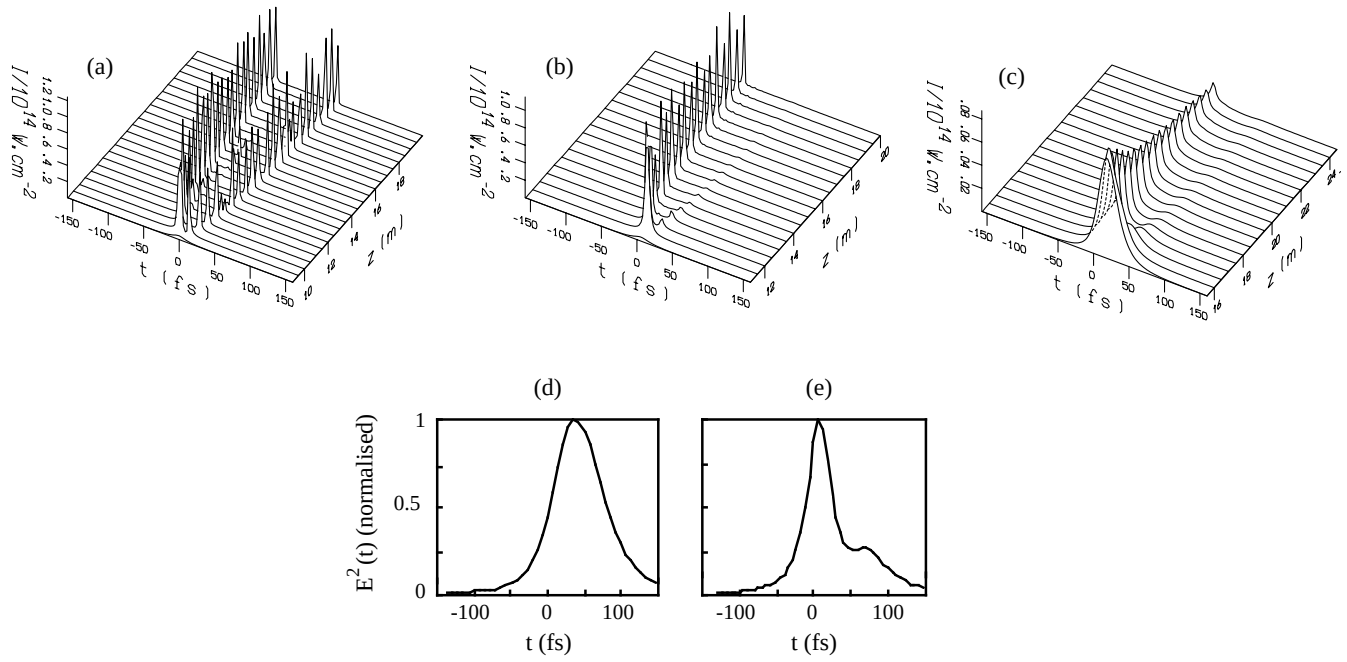

Fig. 10. Temporal shape evolution with the propagation distance z for the three cases corresponding to (a) $r_{\mathrm{K}} = 0$, (b) $r_{\mathrm{K}} = 0.2$ and (c) $r_{\mathrm{K}} = 1$. Temporal shape of the pulse corresponding to $r_{\mathrm{K}} = 1$, with (d) $z = 0.95z_{\mathrm{f}}$ and (e) $z = 1.05z_{\mathrm{f}}$. The field is radially integrated over a 160 μm diameter.

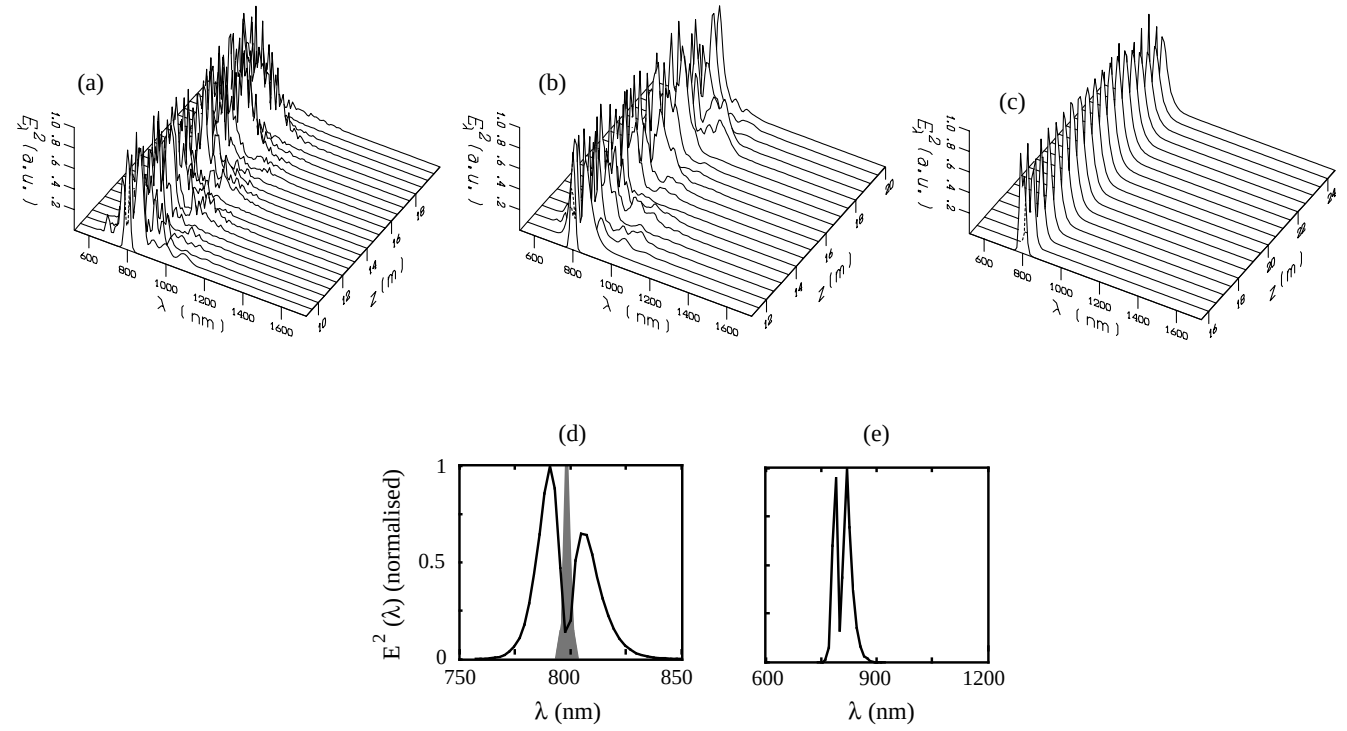

Fig. 11. Spectral shape evolution as a function of the propagation distance z for the three cases corresponding to (a) $r_{\mathrm{K}} = 0$, (b) $r_{\mathrm{K}} = 0.2$ and (c) $r_{\mathrm{K}} = 1$. Spectral shape of the pulse corresponding to $r_{\mathrm{K}} = 1$, with (d) $z = 0.95z_{\mathrm{f}}$ and (e) $z = 1.05z_{\mathrm{f}}$. The field is radially integrated over a 160 μm diameter. The initial spectrum extension is plotted in black in Figure 10(d).

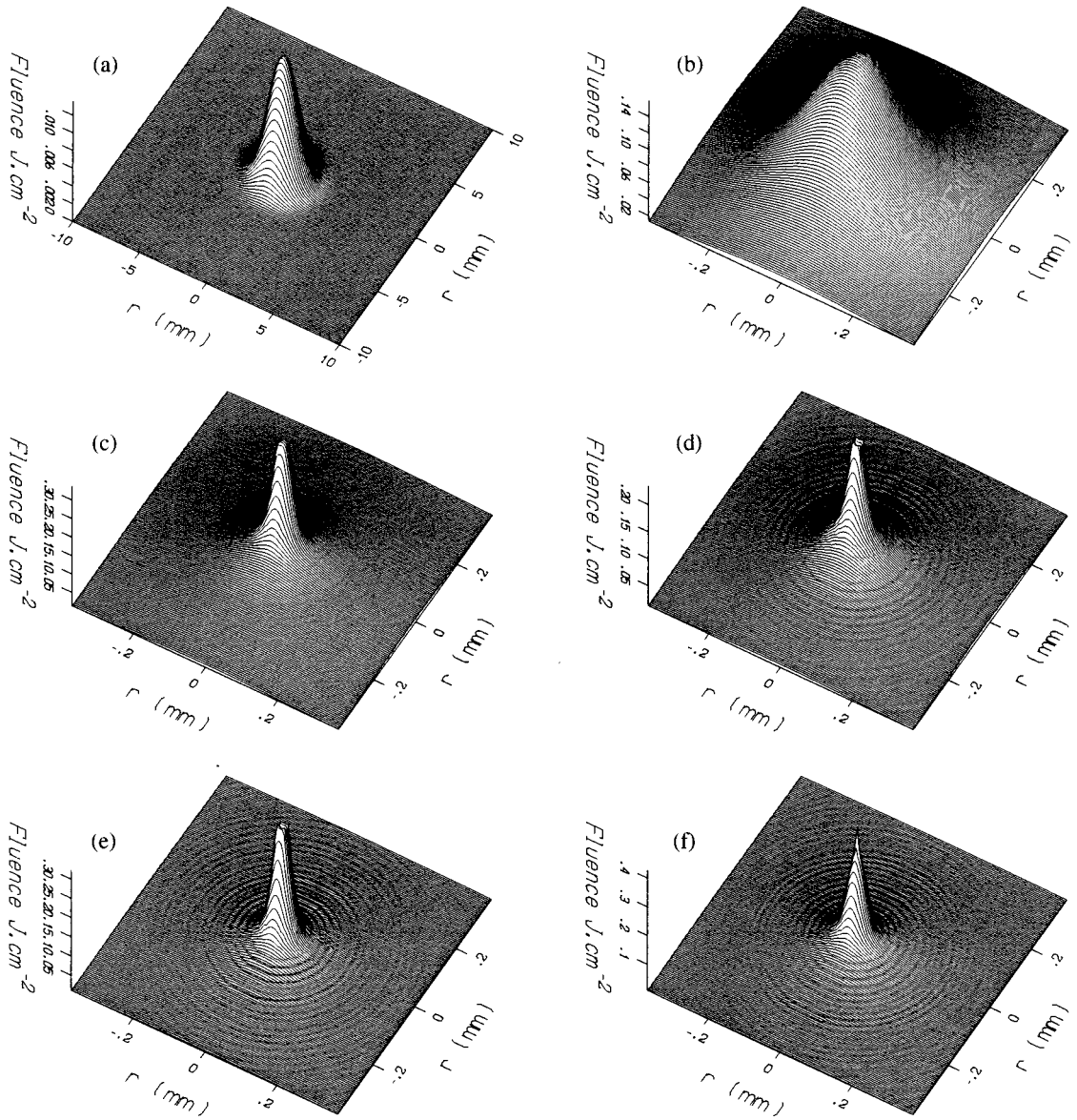

Fig. 12. Collimated beam propagation in air of a 1 mJ, 120 fs pulse. The fluence of the beam is given for different distances before the onset of the filament ($z_f = 6.4$ m) at (a) $z = 0$ m and (b) $z = 6$ m, and after the onset at (c) $z = 8.8$ m, (d) $z = 11.6$ m, (e) $z = 15.8$ m and (f) $z = 16.85$ m. Note the appearance of rings after the onset.

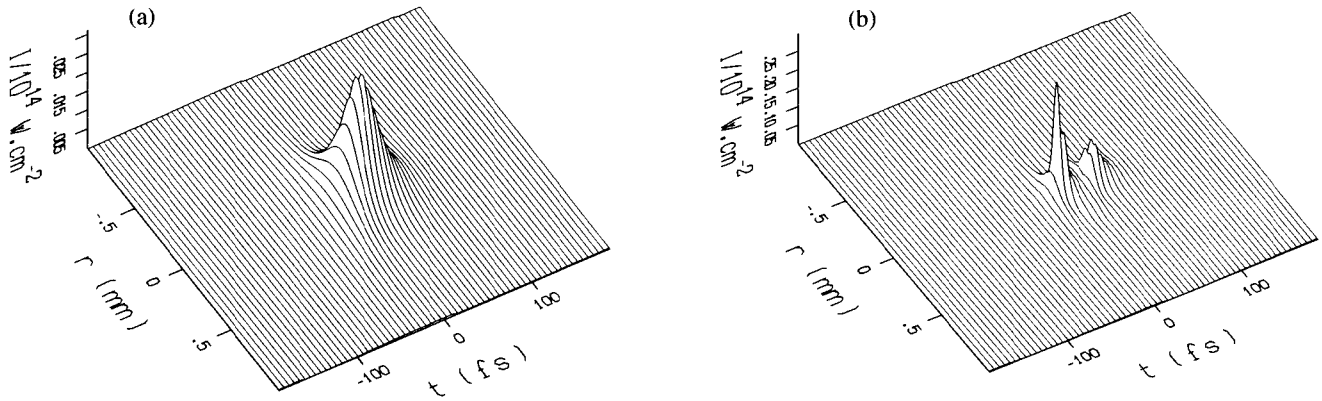

Fig. 13. (a) Time evolution of the pulse shape before the onset of the filament at $z = 6$ m. (b) Time evolution of the pulse shape after the onset of the filament at $z = 6.5$ m.

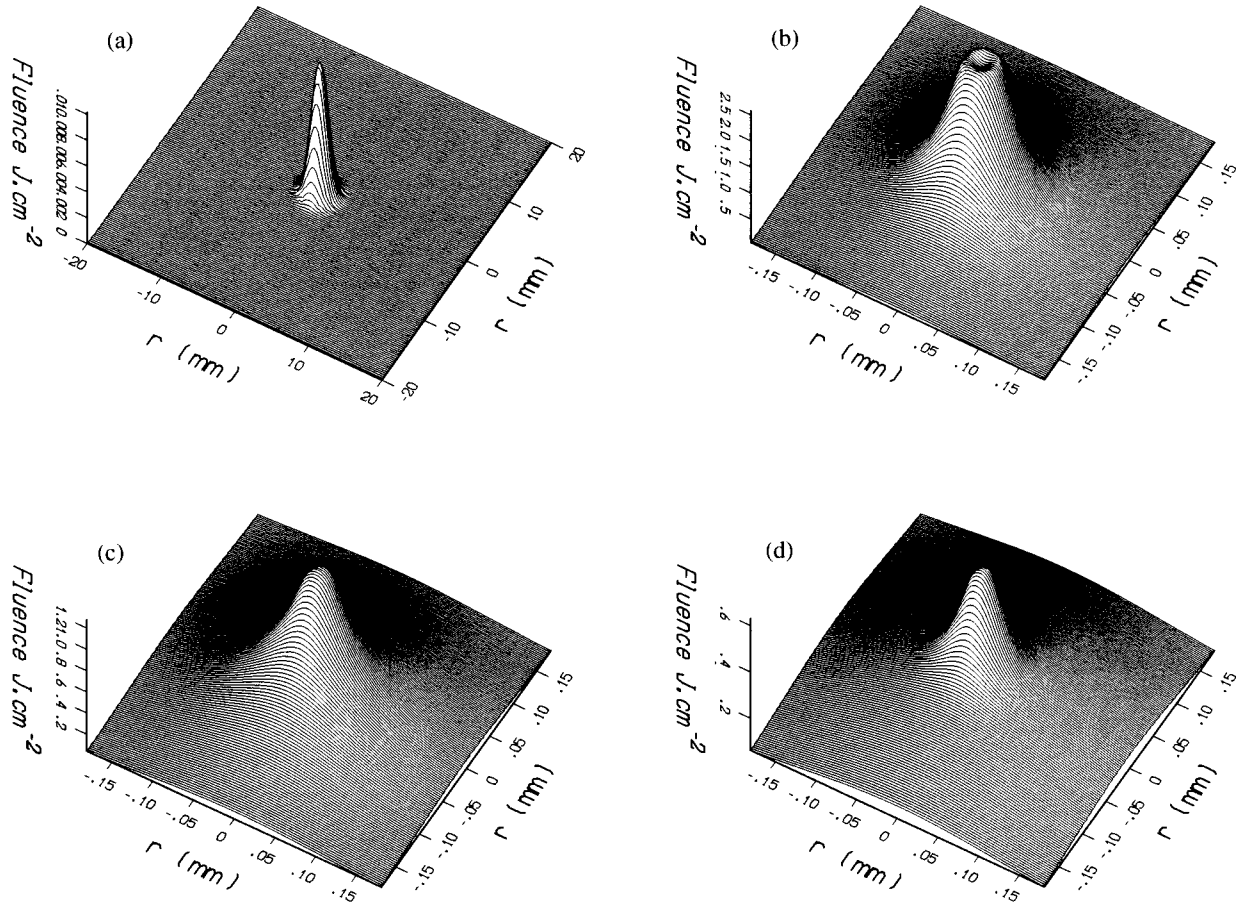

Fig. 14. Converging beam propagation in air of a 1 mJ, 120 fs pulse with a focal length $f = 2$ m. The fluence of the beam is given for different distances before the onset of the filament at (a) $z = 0$ m and after the onset at (b) $z = 1.76$ m, (c) $z = 2.1$ m and (d) $z = 2.3$ m. Note the apparition of a mininum of the central part of the pulse (b) which is reprensentative of a ring.

This is not too surprising, since ionisation acts as a regulator which steps in once the local intensity reaches the threshold-like value necessary for multiphoton ionisation. A fact to be noted is the appearance of a mininum in the central part of the pulse, reflecting a ring pattern. This minimum exists over a few centimeters and then disappears[5].

In Figure 15, two forms of propagation are compared: collimated beam (on the left) and converging beam (right). For each form, the diameter (up) and the corresponding ionisation rate (down) are plotted. As reported above, the diameter presents a similar behavior. The use of a focal length imposes a more homogeneous diameter to the converging beam (Fig. 15(b)) because the focalisation does not permit spatial expansion. The ionisation rate (Fig. 15(c), (d)) fluctuates with distance but is always less than one percent at the center of the beam. If integrated over the beam diameter, the average ionisation rate is reduced to less than 0.1%. This probably explains why it is difficult to observe experimentally the trail of ionised air behind the pulse [41]. One notices surges of the ionisation rate, showing that we deal with a pseudo-dynamic equilibrium between ionisation and Kerr effect, rather than a true dynamic equilibrium, such as occurs in a soliton for instance. The front edges of the ionisation structures are correlated with the decrease of pulse diameter, while the trailing edge corresponds to the increase of the beam diameter. Near the focal point, the ionisation process sets in suddenly to prevent the beam collapse, then decreases within a few centimeters of further propagation of the pulse. It is mainly in this region that ring patterns such as those of Figure 14(b) are generated. The onset of ionisation is recurrent, with quasi-periodic surges occurring over finite distances. By taking the local conditions immediately after the ionisation flash has occured and using equation (20), we can calculate a self-focussing distance of the beam which is compatible with the period of the surges. Therefore, bursts of ionisation are essen-

[5] We tentatively interpret the central minimum (which we observe experimentally) as energy transferred to outer rings. A central minimum appears also with parallel beam geometry, albeit less pronounced (see Fig. 12).

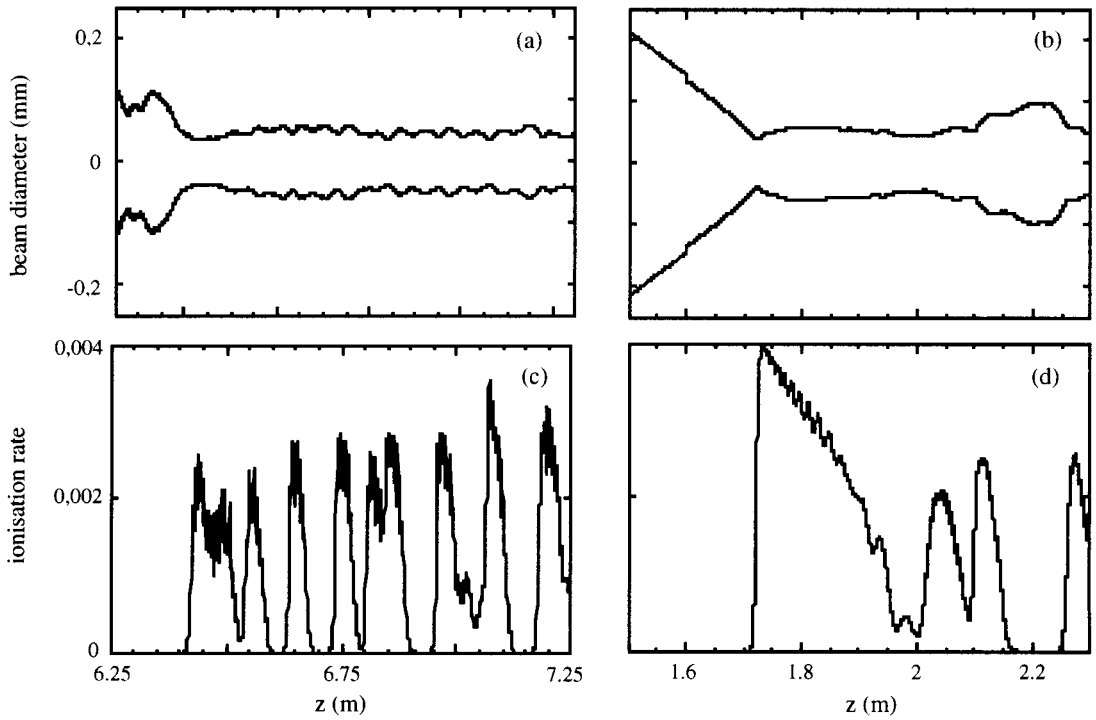

Fig. 15. Pulse diameter (a, b) and associated ionisation rate as a function of the propagation distance for two configurations: (a, c) parallel beam propagation and (b, d) converging beam propagation with a focal length of 2 m.

tial for controlling the self-guiding, dissipating thereby a minimum of energy.

5 Conclusions and perspectives

In this paper, a detailed numerical study of femtosecond pulse propagation in transparent media has been performed. The different nonlinear effects which play a role have been introduced successively, in such a way that their contribution can be better appreciated. In a last stage, simulations performed with conditions approaching those of the usual atmospheric air have revealed an intricate behavior. Effects such as pulse self-shortening, self-focussing and time-splitting occur through the combined effect of the nonlinear Kerr effect and multiphoton ionisation. Self-guided propagation of compressed pulses emerges, with a stable propagation mode over very long distances. The essential role of multiphoton ionisation in this stabilisation process has been pointed out.

In its present form, the code disregards the group velocity dispersion. This restricts its validity to dilute systems far from gas resonance and to distances of a few meters for 100 fs pulses and to distances of a few centimeters for self-compressed self-guided pulses. However, it illustrates the key features leading to measurable pulse changes. An improved code including group velocity dispersion and losses resulting from ionisation is presently developed. This code will necessarily increase the computing time.

We thank Thierry Lehner for discussions on the ionisation model. H. R. Lange gratefully acknowledges the support by a Marie-Curie-Fellowship of the European Community (grant # ERBFMBICT950065). This work has been funded by Training and Mobility of Researchers contracts # ERBFMRXCT96-0080 and # ERBFMGECT950019.

References

1. A. Tünnermann, C. Momma, K. Mossavi, C. Windolph, B. Wellegehausen, IEEE J. Quantum Electron. **29**, 4 (1993); A.B. Borisov, A.V. Borovskiy, V.V. Borobkin, A.M. Prokhorov, O.B. Shiryaev, X.M. Shi, T.S. Luk, A. McPherson, J.C. Solem, K. Boyer, C.K. Rhodes, Phys. Rev. Lett. **68**, 15 (1992); K.H. Yang, Appl. Phys. Lett. **19**, 285 (1971).
2. A. L'Huillier, P. Balcou, S. Candel, K.J. Schafer, K.C. Kulander, Phys. Rev. A **46**, 2778 (1992).
3. Y.R. Shen (editor), *The Principles of Nonlinear Optics* (Wiley-Interscience Publication), ISBN 0-471-88998-9.
4. K. Tamura, M. Nakazawa, Opt. Lett. **21**, 1 (1996); A.T. Ryan, G.P. Agrawal, Opt. Lett. **20**, 3 (1995); Ching-yue Wang, W. Zhang, K.F. Lee, K.M. Yoo, Opt. Commun. **137**, 89 (1997) and references therein; J.E. Rothenberg, Opt. Lett. **17**, 8 (1992); E. Garmire, R.Y. Chiao, C.H. Towbes, Phys. Rev. Lett. **16**, 347 (1966); R.G. Brewer, J.R. Lifsitz, E. Garmire, R.Y. Chiao, C.H. Townes, Phys. Rev. **166**, 326 (1968); J.K. Ranka, R.W. Schirmer, A.L. Gaeta, Phys. Rev. Lett. **77**, 18 (1996).
5. O. Svelto, *Progress in Optics XII*, edited by Wolf (North Holland, Amsterdam, 1974).
6. Y. Silberberg, Opt. Lett. **12**, 1282 (1995).

7. P.M. Goorjian, A. Taflove, R.M. Joseph, S.C. Hagness, IEEE J. Quantum Electron. **28**, 10 (1992); E.E. Fill, J. Opt. Soc. Am. B **11**, 2241 (1994); L. Torner, J.P. Torres, C.R. Menyuk, Opt. Lett. **21**, 7 (1996); S. Trillo, A.V. Buryak, Y.S. Kivshar, Opt. Commun. **122**, (1996) and references therein.
8. Y.R. Shen. Quantum Electron. **4**, 1 (1975).
9. J.H. Marburger. Prog. Quantum Electron. **4** (1975).
10. A. Chiron, G. Bonnaud, A. Dulieu, J.L. Miquel, G. Malka, M. Louis-Jacquet, G. Mainfray, Phys. Plasmas **3**, 4 (1996) and references therein; M.A. Blain, G. Bonnaud, A. Chiron, G. Riazuelo, CEA-Report R-5716 (1996) part I and II.
11. H.S. Brandi, C. Manus, G. Mainfray, T. Lehner, G. Bonnaud, Phys. Fluids B **5**, 3539 (1993); G. Bonnaud, H.S. Brandi, C. Manus, G. Mainfray, T. Lehner, Phys. Plasmas **1**, 968 (1994).
12. A.B. Borisov, X. Shi, V.B. Karpov, V.V. Korobkin, J.C. Solem, O.B. Shiryaev, A. McPherson, K. Boyer, C.K. Rhodes, J. Opt. Soc. Am. B **11**, 1941 (1994).
13. G.P. Agrawal, *NonLinear Fiber Optics*, 2nd Edition *Quantum Electronics, Principles and Applications*, ISBN 0-12-045140-9.
14. V.P. Kandidov, O.G. Kosareva, S.A. Shlenov, Quantum Electron. **24**, 10 (1994); V.P. Kandidov, O.G. Kosareva, S.A. Shlyonov, Nonlinear Opt. **12**, 119 (1995).
15. A. Brodeur, C.Y. Chien, F.A Ilkov, S.L. Chin, O.G. Kosareva, V.P. Kandidov, Opt. Lett. **22**, 5 (1997).
16. O.G. Kosareva, V.P. Kandidov, A. Brodeur, C.Y. Chien, S.L. Chin, Opt. Lett. **22**, 17 (1997).
17. M. Mlejnek, E.M. Wright, J.V. Moloney, Opt. Lett. **23**, 5 (1998); J.K. Ranka, A.L. Gaeta, Opt. Lett. **23**, 7 (1998).
18. P. Mora, T.M. Antonsen jr., Phys. Plasmas **4**, 217 (1997); T.M. Antonsen Jr, P. Mora, Phys. Rev. Lett. **69**, 15 (1997); A. Bendib, A. Tahraoui, P. Chessa, P. Mora, Opt. Commun. **142**, 146 (1997).
19. P. Sprangle, E. Esarey, J. Krall, G. Joyce, Phys. Rev. Lett. **69**, 15 (1997); E. Esarey, P. Sprangle, J. Krall, A. Ting, IEEE J. Quantum Electron. **33**, 11 (1997).
20. P. Chessa, Ph.D. Thesis, Ecole Polytechnique Palaiseau, (1996).
21. P.L. Kelley, Phys. Rev. Lett. **15**, 1005 (1965); V.I. Talanov, JETP Lett. **2**, 138 (1965); S.K. Akhamov, A.P. Sukhorukov, R.V. Khokhlov, JETP **23**, 1025 (1966); S. K. Akhamov, A.P. Sukhorukov, R.V. Khokhlov, JETP **24**, 198 (1967).
22. L.V. Keldysh, JETP **20**, 5 (1965).
23. P.B. Corkum, N.H. Burnett, F. Brunel, Phys. Rev. Lett. **62**, 11 (1989).
24. M.V. Ammosov, N.B. Delone, V.P. Kraïnov, JETP **64**, 6 (1986).
25. S. Augst, D.D. Meyerhofer, D. Strickland, S.L. Chin, J. Opt. Soc. Am. B **8**, 4 (1991).
26. J. Denavit, D.W. Phillion, Phys. Plasmas **1**, 6 (1994).
27. J.P. Heritage, T.K. Gustafson, C.H. Lin, Phys. Rev. Lett. **34**, 21 (1975); C.H. Lin, J.P. Heritage, T.K. Gustafson, R.Y. Chiao, J.P. McTague, Phys. Rev. A **13**, 2 (1976).
28. J.F. Ripoche, G. Grillon, B. Prade, M. Franco, E. Nibbering, R. Lange, A. Mysyrowicz, Opt. Commun. **135**, 310 (1997).
29. M. Scalora, M.E. Crenshaw, Opt. Commun. **108**, 191 (1994); K.J. Blow, D. Wood, IEEE J. Quantum Electron. **25**, 12 (1989); A.S. Kewitsch, A. Yariv, Opt. Lett. **21**, 1 (1996).
30. E.T.J. Nibbering, G. Grillon, M.A. Franco, B.S. Prade, A. Mysyrowicz, J. Opt. Soc. Am. B **14**, 3 (1997).
31. B. Prade, J.M. Schins, E.T.J. Nibbering, M.A. Franco, A. Mysyrowicz, Opt. Commun. **113**, 79 (1994).
32. R. Trebino, D.J. Kane, J. Opt. Soc. Am. A **10**, 5 (1993).
33. M.A. Franco, H.R. Lange, J.F. Ripoche, B.S. Prade, A. Mysyrowicz, Opt. Commun. **140**, 331 (1997).
34. M.M.T. Loy, Y.R. Shen, IEEE J. Quantum Electron. **9**, 3 (1973).
35. S. Carusotto *et al.* Nuovo Cimento D **5**, 328 (1985).
36. A. Braun, G. Korn, X. Liu, D. Du, J. Squier, G. Mourou, Opt. Lett. **20**, 73 (1195).
37. G. Mourou, Opt. Lett. **20**, 73 (1995).
38. E.T.J. Nibbering, P.F. Curley, B.S. Prade, M.A. Franco, F. Salin, A. Mysyrowicz, Opt. Lett. **21**, 1 (1996); E.T.J. Nibbering, M.A. Franco, B.S. Prade, G. Grillon, J.P. Chambaret, A. Mysyrowicz, J. Opt. Soc. Am. B **13**, 2 (1996)
39. E.T.J. Nibbering, M.A. Franco, B.S. Prade, G. Grillon, C. Le Blanc, A. Mysyrowicz, Opt. Commun. **119**, 479 (1997).
40. H.R. Lange, G. Grillon, J.F. Ripoche, M.A. Franco, B. Lamouroux, B.S. Prade, A. Mysyrowicz, E.T.J. Nibbering, A. Chiron, Opt. Lett. **23**, 2 (1998).
41. H. Nishioka, W. Odajima, K.I. Ueda, H. Takuma, Opt. Lett. **20**, 24 (1995).